RSC Advances

PAPER

View Article Online
View Journal | View Issue

Cite this: *RSC Adv.*, 2015, **5**, 82717

Tailoring the structure and gas permeation properties of silica membranes *via* binary metal oxides doping†

P. H. Tchoua Ngamou,*[a] M. E. Ivanova,[a] C. Herwartz,[b] N. Lühmann,[c] A. Besmehn,[c] W. A. Meulenberg,[a] J. Mayer[bd] and O. Guillon[a]

Received 6th August 2015
Accepted 24th September 2015

DOI: 10.1039/c5ra15783h

www.rsc.org/advances

The sol–gel method was employed for the synthesis of binary X–Co (X: Mn, Cr) oxide-doped silica membranes with different X/Co molar ratios (X/Co: 0.1, 0.3, 0.9). Single-gas permeation tests were performed at 200 °C to determine the effect of the binary oxide composition on the amorphous silica network. The X-ray diffraction (XRD), X-ray Photoelectron Spectroscopy (XPS) and Transmission Electron Microscopy (TEM) indicated the presence of smaller $Mn_xCo_{3-x}O_4$ and $Cr_xCo_{3-x}O_4$ oxide nanocrystals in the silica matrix in addition to amorphous Co, Mn and Cr species. The H_2/N_2 permeance ratio decreased from (126.3 ± 9) to (10.7 ± 2) with an increase in X/Co molar ratio from 0.1 to 0.9 due to the formation of larger pores. However, the binary Co–X oxide-doped silica membrane with the lowest X content showed a H_2/N_2 permeance ratio, (126.3 ± 9), higher than that, (63.6 ± 6), of the single cobalt oxide silica membrane. Based on FTIR analysis, it was found that the densification of the membrane at low X content resulted from the formation of silica structures with narrowed siloxane rings. In contrast, the enlargement of siloxane rings due to favorable condensation reactions occurred at high X content.

Introduction

Systems based on transition-metal oxide nanoparticles embedded in inorganic oxide matrices are receiving growing interest in innovative technological applications. The combination of the unique properties of the guest phase and the host matrix is at the origin of the discovery of new or improved properties. For example, cobalt oxide nanoparticles dispersed in a high surface area silica matrix represents one of the most investigated functional composite materials thanks to its catalytic[1–3] and gas/humidity sensing[4,5] properties. In the field of membrane technology for H_2 purification from gas mixtures, embedding cobalt oxide nanoparticles into a silica matrix has been demonstrated to improve both the stability and the separation performance of the silica membrane in presence of steam.[6,7] The poor hydrothermal stability of silica membranes is ascribed to the rearrangement of the silica structure *via* hydrolysis and condensation reactions, which lead to a membrane densification and eventually to the formation of cracks and larger non-selective pores. The presence of dispersed Co_3O_4 nanoparticles within the silica framework was believed to shield the silica matrix and inhibit the hydrolysis and condensation of the silica in the pore walls, thereby limiting the structural rearrangement.[8,9] This was not the case of TiO_2, Nb_2O_5 and ZrO_2 oxides, which improve the hydrothermal stability of the silica by stabilizing the porous structure *via* enhancement of network connectivity.[10] Cobalt oxide-doped silica membranes have also been demonstrated to be stable in the presence of H_2S[11] as well as in aqueous environments, as for example during the long-term pervaporation dehydration of ethanol–water mixture.[12] The literature, as above-mentioned, clearly shows that cobalt oxide is the most investigated transition metal oxide in producing metal oxide silica membranes for gas separation. Some attempts have been made with FeO_x but the obtained membranes, although microporous were not suitable for gas separation,[13] whilst thermally stable oxides such as CrO_x and MnO_x were embedded on SBA-15 mesoporous silica structures for catalytic application.[14,15]

Very recently, the incorporation of binary metal oxides within the silica framework has been shown to affect the separation properties of the membrane. For example, Ballinger *et al.*[16] reported a decrease of gas separation properties of binary palladium–cobalt oxides silica membranes after exposure at 500 °C in presence of hydrogen. The reduced gas separation

[a]*Institute for Energy and Climate Research, IEK-1: Materials Synthesis and Processing, Forschungszentrum Jülich GmbH, 52425 Jülich, Germany. E-mail: p.tchoua@fz-juelich.de*

[b]*Central Facility for Electron Microscopy (GFE), RWTH Aachen University, 52056 Aachen, Germany*

[c]*Central Institute for Engineering, ZEA-3: Analytics, Forschungszentrum Jülich GmbH, 52425 Jülich, Germany*

[d]*Ernst Ruska-Centre for Microscopy and Spectroscopy with Electrons ER-C, Forschungszentrum Jülich GmbH, D-52425 Jülich, Germany*

† Electronic supplementary information (ESI) available. See DOI: 10.1039/c5ra15783h

performance was attributed to the easy reducibility of the palladium oxide to its metallic state, which creates molecular gaps into the silica matrix. In a separate study,[17] the same authors reported an enhancement of gas separation properties of binary lanthanum–cobalt oxides silica membranes after redox cycling. This improvement of the gas separation properties was ascribed to the closure or collapse of large pore sizes, most likely influenced by the presence of the lanthanum silicate phase. Darmawan *et al.*[18] demonstrated that the gas separation properties of iron–cobalt oxide membranes were affected by changing the Fe/Co molar ratio, and enhanced gas permeance and permeation ratios where obtained for Fe/Co = 0.1. However, a correlation between the gas separation properties and the structural parameters was not demonstrated. In fact, the spinel Co_3O_4 can accommodate various cations with more than one oxidation state within the available octahedral and tetrahedral sites. This structural tailorability of Co_3O_4 has been demonstrated to be at the origin of interesting and tunable properties.[19] Therefore, the insertion of other transition metal oxides such as MnO_x and CrO_x in the lattice of the spinel Co_3O_4 can structurally affect the silica network and hence the separation performance of the membrane.

In this context, the present work aims to investigate the effect of the incorporation of binary metal oxides X–Co (X = Mn, Cr) with different compositions into the silica matrix. As the metal oxide concentration into the silica matrix is well-known to affect the membrane performance,[6] the total metal-to-silicon molar ratio was kept constant during the sols synthesis and only X/Co molar ratio was varied. Structural and chemical changes induced by the incorporation these binary oxides were analyzed by means of X-ray diffraction (XRD), X-ray Photoelectron Spectroscopy (XPS), Transmission Electron Microscopy (TEM), Fourier Transform Infrared (FTIR) and discussed together with the single gas permeation results. Furthermore, the gas permeation properties of these binary oxides silica membranes were compared to that of a reference single cobalt oxide silica membrane. Cobalt oxide has been used as one component of the binary metal oxide because it is recognized to improve the hydrothermal stability of the silica membrane. We have decided to concentrate first on the structural modification induced by the insertion of these binary oxides and their influence on the separation performance. The long-term hydrothermal stability of these binary membranes will be investigated in the next step of this research work.

Experimental

Sol–gel synthesis

The sol–gel technique was employed for the preparation of binary X–Co (X = Mn, Cr) metal oxide-doped silica sols with different X/Co molar ratios (X/Co = 0.1, 0.3 and 0.92), while keeping the total metal-to-silicon ratio constant *i.e.* (Co + X)/Si = 1 : 2. The acid catalyzed sol–gel method used in this study is a modified version of the procedure previously reported for pure SiO_2 by van Gestel *et al.*[20] In brief, tetraethylorthosilicate (TEOS) was mixed with ethanol at room temperature and an aqueous solution of nitric acid was added dropwise. The obtained transparent solution was refluxed at 60 °C for 3 h to promote hydrolysis and condensation reactions. Then, the corresponding amounts of cobalt nitrate hexahydrate ($Co(NO_3)_2 \cdot 6H_2O$) and chromium nitrate nonahydrate ($Cr(NO_3)_3 \cdot 9H_2O$) or cobalt nitrate hexahydrate ($Co(NO_3)_2 \cdot 6H_2O$) and manganese nitrate tetrahydrate ($Mn(NO_3)_2 \cdot 4H_2O$) were dissolved in ethanol and added slowly to the transparent solution. The obtained sols were refluxed at 60 °C for 5 h and the final molar ratio of different components TEOS : metal nitrate hydrate : EtOH : H_2O : HNO_3 was 2 : 1 : 7.6 : 12.3 : 0.09. During the synthesis, the (X + Co)/Si molar ratio was kept equal to 1 : 2 and X/Co molar ratio (hereafter denoted as XCoSi-a where a = X/Co) was 0 : 100; 10 : 90; 25 : 75 and 48/52.

Powder preparation and characterization

The obtained sols were dried in an oven at 60 °C for 72 h to form xerogels. The xerogels samples were ground into a fine powder and fired in air at 600 °C for 3 h using a heating/cooling rate of 1 °C min^{-1}. Several analytical techniques such as XRF, FTIR, XRD, XPS, TEM have been employed for the characterization of the prepared powders. Elemental analysis of the binary metal oxide-doped silica powders were performed by means of a dispersive X-ray fluorescent instrument (Bruker S8 Tiger). Infrared spectroscopy was performed using a Tensor 27 (Bruker Optics) equipped with an DTGS detector and a Golden Gate diamond attenuated total reflectance (ATR) unit containing ZnSe mirrors. The resolution of the spectrometer was set at 4 cm^{-1} and all spectra were collected in the range 800–4000 cm^{-1} and normalized to the gradient vector for comparison. The deconvolution of the absorption bands was performed using the "fit multiple peaks" function of the ORIGIN Pro 9.0 software. Only the peak position of the Si–OH vibration was fixed at 950 cm^{-1}, while the peak position and peak height of other components were allowed to vary between samples to achieve the best possible fit. A D4 Endeavor Bruker AXS diffractometer with a Kristalloflex 770 X-ray generator was used to record the XRD patterns. A Pawley fit using the "Topas 4.2" software was used for the identification of the crystalline phases by referring to the powder XRD database JCPDS-ICDD and the calculation of the lattice parameter, while the crystalline sizes were calculated using the Scherrer equation. X-ray photoelectron spectroscopy (XPS) measurements were performed using a PHI5000 Versa Probe II from ULVAC-PHI Inc., USA, equipped with an Al k-alpha (1.486 KeV) source for excitation in the analysis chamber under high vacuum (1×10^{-8} mbar). The sample charging was corrected with respect to the binding energy of the C1s core level (284.6 eV). The peak deconvolution was achieved using the "fit multiple peaks" function of the ORIGIN Pro 9.0 software. The fitting of synthetic components followed the procedures described by Biesinger *et al.*[21]

The surface and cross-section images of membranes were obtained using a Zeiss ultra 55 scanning emission microscope operating at an accelerating voltage of 15 KV. A transmission electron microscope (FEI Tecnai F20) equipped with an EDAX EDX system and a GATAN GIF imaging filter was used for the identification of the morphology and crystal structure of the

prepared powders. TEM samples were prepared by suspending the powders on a holey carbon grid.

Membrane fabrication and testing

Prior to dip-coating, the sols were diluted 15 times in ethanol and filtered with a 0.8 μm membrane filter (Whatman FP30/0.8CA). A series of 2 mm-thick α-Al_2O_3 disk-shaped supports provided by Pervatech BV (39 mm diameter) were dip-coated with a boehmite sol as describe elsewhere.[20]

After calcination at 600 °C for 3 h, a γ-Al_2O_3 intermediate layer with an average pore size of 5 nm was formed. Binary metal oxide-doped silica membranes were prepared by dip-coating the ceramic supports in ethanol-diluted sols using an automatic dip coater (KSV NIMA). The membrane calcination procedure was identical as for powders. The coating and calcination cycle steps were repeated to increase the film thickness and cover any remaining defects. Gas permeation tests were performed using an in-house made dead-end mode stainless steel module. The gas flow at the feed side of the module was controlled by an accurate pressure controller (Brooks, pressure controller 5866). The gas flow rate at the permeate side was measured using two flow meters with maximum flow of 8 ml min^{-1} and 40 ml min^{-1} (Brooks, smart mass flow).

Discussion and results

Gas permeation properties of binary metal oxides-doped silica membranes

Fig. 1 shows a typical SEM image of the surface and cross-section of the manganese-cobalt oxide-doped silica membrane with a Mn/Co molar ratio of 0.9 (named MnCoSi-0.9). A 120 nm-thick and uniform MnCoSi top layer, coated on a γ-Al_2O_3 interlayer, can clearly be observed. The gas separation performance of sol–gel made CoSi and XCoSi (X = Mn, Cr) membranes was evaluated by measuring the permeance at 200 °C of several gases with different kinetic diameters. The measured permeance values in addition to H_2/N_2 permeance ratios are presented in Fig. 2(a–c) and Table S1 of the ESI.† A test series of five samples were performed for each membrane with a good reproducibility of gas permeance, thereby confirming the reproducibility of the sol–gel synthesis method. A close examination of gas permeance values displayed in Fig. 2(a–c) indicates that the combination of binary X–Co (X = Mn, Cr)

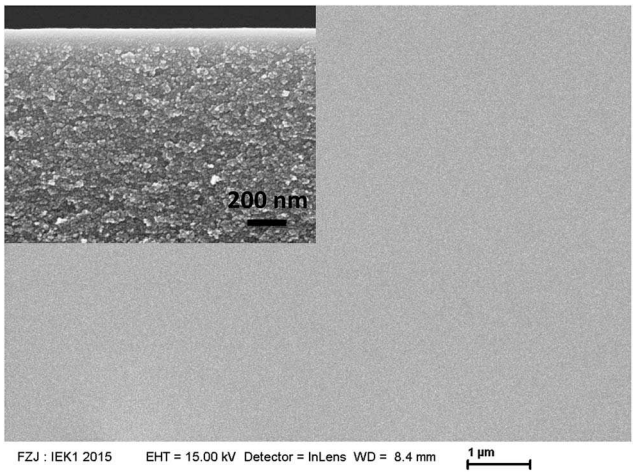

Fig. 1 SEM picture of the MnCoSi-0.1 film top layer. The insert corresponds to the cross-sectional SEM image of the ceramic membrane, showing the intermediate gamma alumina layer and the 120 nm thick MnCoSi-0.1 top layer.

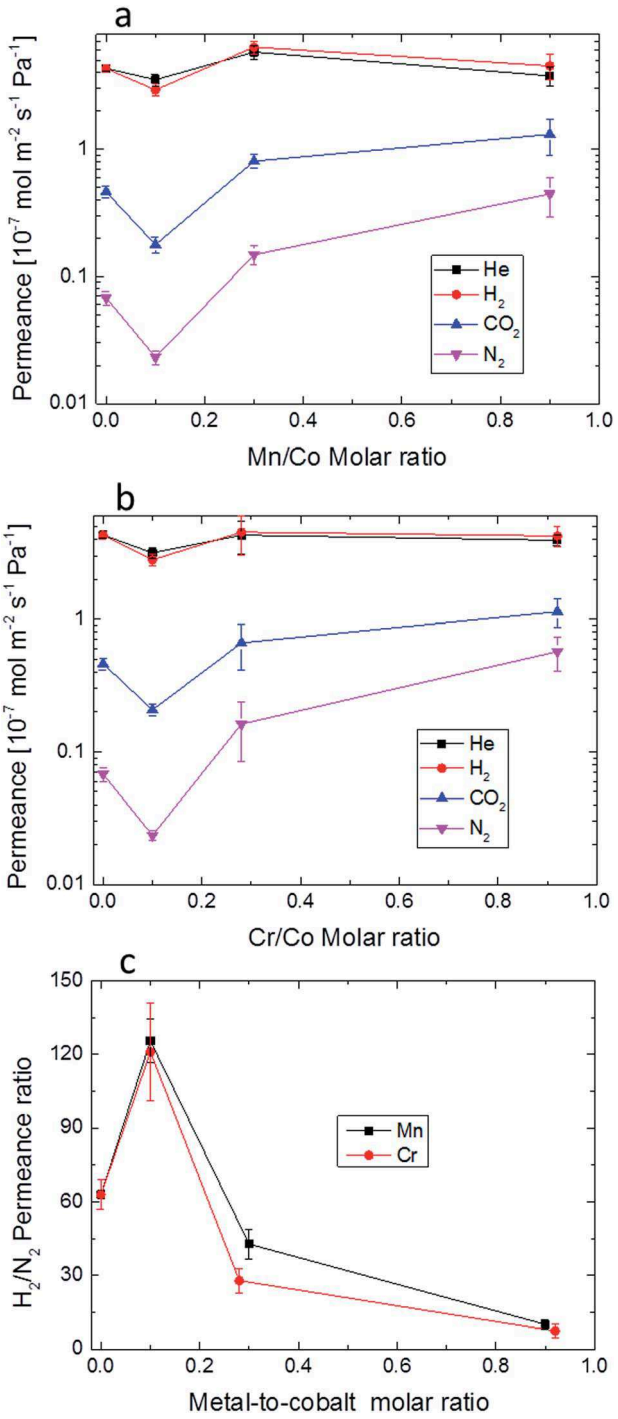

Fig. 2 (a and b) Gas permeance (He, H_2, CO_2, N_2) and (b) H_2/N_2 permeance ratio as function of the X/Co (X = Mn, Co) molar ratio.

oxides into the silica matrix enabled the formation of silica structures with different pores sizes. This was highlighted by the permeance of large gas molecules like CO_2 ($d_k = 0.33$ nm) and N_2 ($d_k = 0.36$ nm), which increased with an increase in X content. For example, the N_2 permeance increased from $(2.3 \pm 0.3) \times 10^{-9}$ mol m^{-2} s^{-1} Pa^{-1} to $(4.4 \pm 0.2) \times 10^{-8}$ mol m^{-2} s^{-1} Pa^{-1} and from $(2.3 \pm 0.2) \times 10^{-9}$ mol m^{-2} s^{-1} Pa^{-1} to $(5.7 \pm 0.2) \times 10^{-8}$ mol m^{-2} s^{-1} Pa^{-1} as the Mn/Co and Cr/Co molar ratios increased from 0.1 to 0.9, respectively. This increase of the N_2 permeance for more than one order of magnitude is ascribed to the formation of larger pore sizes.

In contrast, CoSi membrane showed at 200 °C a N_2 permeance of $(6.8 \pm 0.8) \times 10^{-9}$ mol m^{-2} s^{-1} Pa^{-1} that is higher than that of XCoSi-0.1 (X = Mn, Cr) membranes. These results suggest that the densification of the silica membrane takes place at low X content (*i.e.* X/Co = 0.1), while the formation of larger pores occurs at higher X content. These findings were confirmed by the behavior of H_2/N_2 permeance ratios as a function of the doping content (Fig. 2(c)). For instance, the CoSi membrane showed H_2/N_2 permeance ratio of 63.6 ± 6 that increased to 126.3 ± 9 for MnCoSi-0.1 membrane, while MnCoSi-0.3 and MnCoSi-0.9 membranes showed H_2/N_2 permeance ratios of 43.6 ± 6 and 10.7 ± 2, respectively. The formation of silica structures with different pore sizes when increasing the X/Co molar ratio can also be evidenced by the permeance of small molecules like He ($d_k = 0.26$ nm) and H_2 ($d_k = 0.289$ nm) as shown in Fig. 2(a) and (b). The permeance of H_2 appeared to be slightly lower than that of He for XCoSi-0.1 membrane and higher than that of He for XCoSi-03 and XCoSi-0.9 membranes. In fact, when the permeation is governed by an activated permeation mechanism, the permeance of H_2 appears lower than that of He due to its high molecular size. In the case of a Knudsen diffusion mechanism, the H_2 permeance is higher than that of He due to the difference in molecular weight. This means that increasing the X/Co molar ratio enables the formation of membranes with pores sizes bigger than the molecular size of H_2 but still lower than the molecular size of N_2. However, low X/Co molar ratio enable the formation of narrower pore sizes than those of the single cobalt oxide-doped silica (CoSi) membrane.

Characterization of binary metal oxides-doped silica gels

Several characterization techniques have been investigated to understand the changes in the silica matrix induced by the insertion of binary Co–Cr and Co–Mn oxides. For the above-mentioned investigations, dried gels were prepared by following the same calcination procedure as for membranes.

Quantitative (XRF) analysis

Quantitative analysis of Co Mn and Cr elements in the CoSi and XCoSi (X = Mn, Cr) powders were done using dispersive X-ray Fluorescence Spectrometry (XRF). The composition of the sol–gel made powders is reported in Table 1. For instance, Mn/Co ratios of 0.1, 0.3 and 0.9 were obtained when maintaining the $Mn(NO_3)_2 \cdot 4H_2O/Co(NO_3)_2 \cdot 6H_2O$ feeding ratios of the precursors at 0.11, 0.33 and 0.92, respectively. The measured values of X/Co and (X + Co)/Si ratios were found to be closed to the nominal ones, showing less than 5% variation.

Table 1 Quantitative analysis of Mn, Cr, Si and Co in all samples determined

Samples	Si (wt%)	Co (wt%)	X (wt%)	X[b]/Co	(X + Co)/Si
CoSi	68.4	31.5	—	—	0.46 (0.5)
MnCoSi-0.1	67.8	29.3	2.90	0.1 (0.11)[a]	0.48 (0.5)
MnCoSi-0.3	66.9	25.5	7.60	0.3 (0.33)	0.49 (0.5)
MnCoSi-0.9	68.6	16.6	14.80	0.9 (0.92)	0.46 (0.5)
CrCoSi-0.1	67.5	29.1	3.40	0.11 (0.11)	0.48 (0.5)
CrCoSi-0.3	68.3	24.7	6.80	0.28 (0.33)	0.46 (0.5)
CrCoSi-0.9	66.3	17.5	16.10	0.92 (0.92)	0.50 (0.5)

[a] The nominal values are within brackets. [b] X represents Mn or Cr according to the sample name.

This indicates that the changes observed during single-gas permeation measurements cannot be ascribed to the difference in the total concentration of binary metal oxides in the silica matrix, but to a variation of X/Co molar ratio.

The formation of silica with different micro-structures upon the variation of X/Co molar ratio was also confirmed by the measurement of the BET surface area by means of N_2 adsorption-technique. We are aware that the N_2-adsorption technique is not representative of the surface area accessible by H_2 but can give information of the general texture of the membrane.[22] The BET surface area of the CoSi sample was found to be 164 m^2 g^{-1}, a value that decreased to 155 m^2 g^{-1} with an increase of Mn/Co to 0.1 due to the densification of the sample.

A further increase of the Mn/Co molar ratio from 0.3 to 0.9 resulted in an increase of the BET surface area from 196 m^2 g^{-1} to 235 m^2 g^{-1}, indicating the formation of more porous structures.

Crystallization and phase information

The XRD patterns at room temperature for the CoSi and XCoSi (X = Mn, Cr) powders are displayed in Fig. 3(a) and (b). The diffraction pattern of the CoSi powder exhibits reflections corresponding to the face centered cubic *Fd3m* spinel-type phase (ICCD-PDF-Nr: 01-080-1536) with a lattice parameter of 0.8084 nm, indicating the presence of crystalline spinel Co_3O_4 phases into the silica matrix. Upon doping with Mn or Cr, the cubic *Fd3m* spinel structure is retained and the diffraction peaks shift to lower angles. The shift to lower angles of diffractions peaks is an indication of the insertion of Mn and Cr ions into the lattice of the spinel Co_3O_4. This was also confirmed by the increase of the lattice parameter (see Table S2†) from 0.8084 nm to 0.8255 nm and 0.8263 nm with an increase in Mn/Co and Cr/Co molar ratios from 0 to 0.92, respectively. The increase of the lattice parameter with the doping content can be well understood by considering the difference in ionic radii of Co, Mn and Cr ions (Co^{2+}: 0.65 pm, Co^{3+}: 0.54 pm, Mn^{2+}: 0.67 pm, Mn^{3+}: 0.65 pm and Cr^{3+}: 0.62 pm). It is more likely that the substitution of Co^{3+} (0.54 pm) by larger Cr^{3+} (0.62 pm) and Mn^{3+}

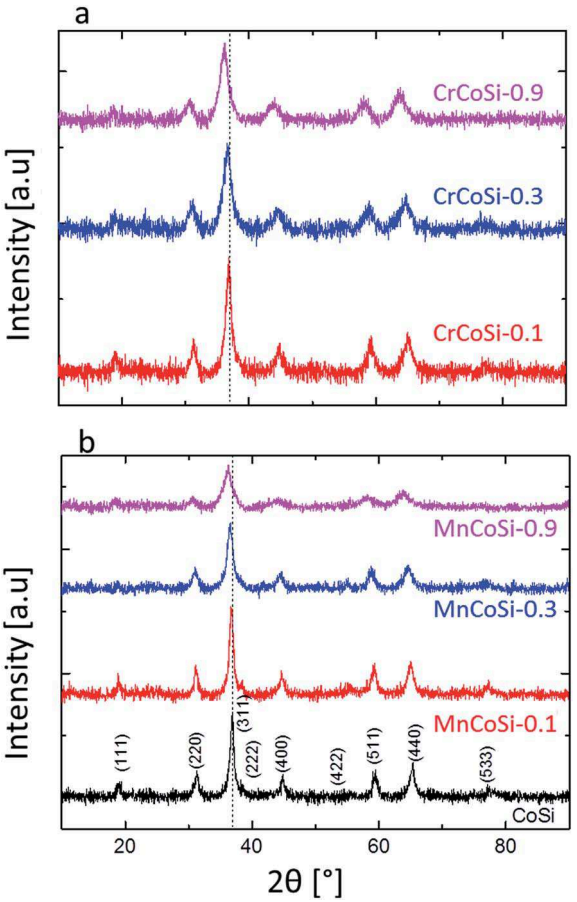

Fig. 3 XRD patterns of CoSi and XCoSi (X = Mn, Cr) samples with different X/Co molar ratios. The background of the XRD patterns was subtracted using the Origin Pro 9 software.

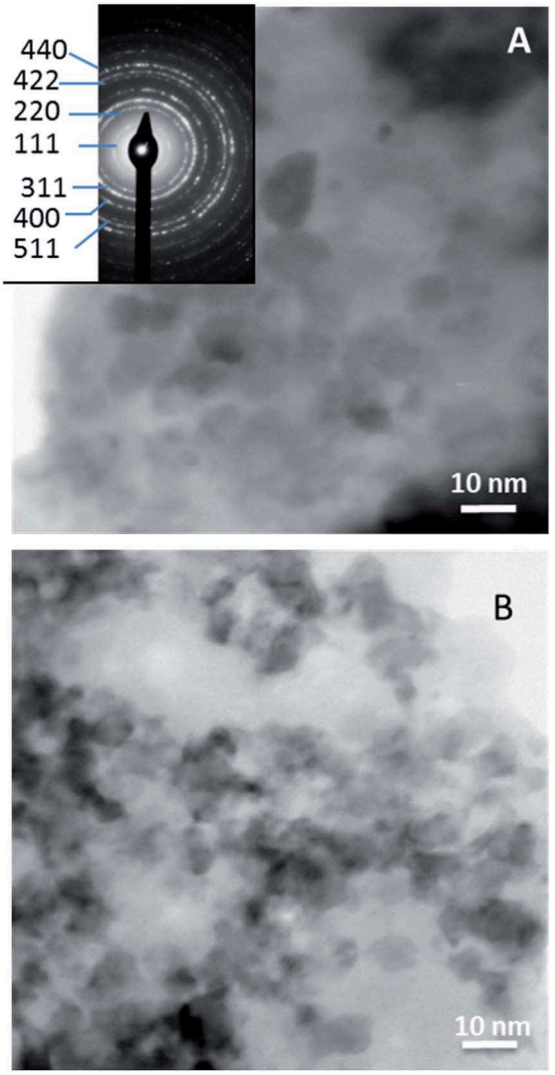

Fig. 4 XRD representative bright-field TEM images and electron diffraction pattern (insert) of the MnCoSi-0.1 sample of the sample (see Fig. S2†).

(0.65 pm) cations in the octahedral site of the spinel Co_3O_4 is responsible for the enlargement of the unit cell.

The average crystalline size of these nanoparticles was estimated using the Scherrer equation and reported in Table S2.† An obvious decrease of the crystalline size with increasing the Mn or Cr content was noticed. For example, the CoSi sample showed an average crystalline size of 9.31 ± 0.5 nm that decreased to 3.68 ± 0.8 nm and 4.5 ± 1.0 nm for MnCoSi-0.9 and CrCoSi-0.9 samples, respectively. It is worth mentioning that no crystalline phases corresponding to MnO_x or CrO_x oxides were observed in the XRD patterns. However, as it will be later shown, the formation of amorphous species into the silica matrix cannot be ruled out.

Morphological (TEM) analysis

Fig. 4 shows representative bright-field (BF) TEM micrographs and the electron diffraction pattern of MnCoSi-0.1 powder. The BF micrographs show that the MnCoSi-0.1 sample is composed of nanocrystalline particles with diameter less than 10 nm, in agreement with the XRD results. The nanocrystals appear not to be very well distributed in the silica matrix as some empty places and agglomeration of tiny crystals can be observed. A close examination of the selected area diffraction pattern (insert in Fig. 4(a)) reveals a total of nine characteristic diffraction rings. As reported in Table S3,† the ratio of the diameter of the diffraction rings (D_1/D_i) was observed to be consistent with the ratio of *d*-spacing (d_1/d_i) obtained from the reflections corresponding to the face centered cubic *Fd3m* spinel-type Co_3O_4 phase (ICCD-PDF-Nr: 01-080-1536). These results confirm the nanocrystalline nature and the *Fd3m* face centered cubic symmetry of the nanoparticles. The EDX analysis of some selected nanoparticles from the TEM micrographs of MnCoSi-0.1 (see Fig. S1†) only revealed the presence of Co, while Co and Mn were detected in the matrix of MnCoSi-0.1 powder. These results suggest that not only Co_3O_4 nanocrystals are present in the silica matrix of MnCoSi-0.1 powder but also some amorphous Co and Mn species, which were undetectable by XRD analysis. This is in agreement with the work of Esposito *et al.*[23] who reported that beside nanocrystalline Co_3O_4 particles, amorphous Co^{2+} ions strongly bonded to the silica matrix were formed during the sol–gel preparation of CoSi powders. It is

worth mentioning that XRD results have indicated an increase of the lattice parameter from 0.808 nm (CoSi) to 0.811 nm (MnCoSi-0.1). Therefore, the non-detection of Mn by analysing the nanoparticle of MnCoSi-0.1 powder might be explained by its relative low quantity that is under the detection limit of the EDX set-up.

Chemical (XPS) analysis

The possible variations in oxidation states of the elements Co, Mn and Cr in the prepared samples were assessed from XPS measurements by analyzing Co2p, Cr2p, Mn2p and Mn3s core shell spectra. The Co2p high-resolution spectra of the CoSi and CrCoSi powders with different Cr/Co ratios are shown in Fig. 5.

The Co2p spectra consist of two main spin-orbital lines, $2P_{3/2}$ and $2p_{1/2}$, separated by about 15 eV.[24–26]

The peak at 779.59–779.25 eV is assigned to Co^{3+} in octahedral sites, while the peak at 780.80–781.55 is attributed to Co^{2+} in tetrahedral sites of the spinel Co_3O_4.[25] The satellite peaks S1 and S2, located at 5–6 eV and 9–10 eV above the main $Co2p_{3/2}$ line, are associated with Co cations having a valence of +2 and +3, respectively.[26] A similar deconvolution was done for MnCoSi powders and quantitative details regarding the peak fittings are summarized in Table S4.† For all the samples it can be seen that the satellite peak S2 is much weaker than S1, indicating a predominance of Co^{2+} ions over Co^{3+}. The fitted Co^{3+}/Co^{2+} value for the CoSi is 0.80, which is far from the expected value, 2, for stoichiometric Co_3O_4 but in agreement with the value, 0.9, reported for sol–gel made CoO_x–SiO_2 xerogels.[8] This low Co^{3+}/Co^{2+} value confirms the presence of others amorphous Co^{2+} species besides the crystalline Co_3O_4 spinel, which is agreement with TEM results. The fitted Co^{3+}/Co^{2+} ratio is noted to decrease from 0.73 to 0.40 and from 0.68 to 0.31 as the Mn/Co molar ratio increase from 0.1 to 0.9, respectively. The decrease of Co^{3+}/Co^{2+} ratio with increasing doping content confirms the information obtained from XRD measurements *i.e.* the substitution of Co^{3+} by larger Mn and Cr ions.

The Mn3s and Mn2p high resolution spectra, Fig. 6(a) and (b), were analyzed to determine the oxidation state of Mn. The doublet of the Mn3s peak is a result of the parallel spin coupling between electrons in the 3s and 3d orbital and the energy separation between the two peaks is closely related to the mean oxidation state of Mn.[26] The splitting widths and the mean oxidation state of Mn ions are provided in Table S5.† The splitting width values were obtained from the deconvolution of Mn3s core shell spectra, Fig. 6(a), while the mean oxidation state of Mn ions were determined from a linear relationship between the splitting width and the mean oxidation state of Mn obtained from the literature.[27] The Mn3s peak splitting width decreased from 5.73 to 5.42 with an increase in Mn content. The decrease of the peak splitting width corresponds to an increase of the mean Mn oxidation state from 2.10 to 2.75, *i.e.* Mn exist in MnCoSi samples as Mn^{2+} and Mn^{3+} ions.

The deconvolution of the $Mn2p_{3/2}$ peak, Fig. 6(b), shows the presence of two components Mn^{2+} and Mn^{3+}, in agreement with the oxidation states predicted from resolved Mn3s spectra. The fitted Mn^{3+}/Mn^{2+} ratio increased from 0.55 to 1.03 with the increase in Mn content, indicating the formation of Mn^{3+} ions at the expense of Mn^{2+}. The presence of Mn^{2+} in MnCoSi samples is not surprising when considering the nature of the starting precursor: Mn $(NO_3)_2 \cdot 4H_2O$. We believe that amorphous Mn^{2+} ions are dispersed in the silica matrix and only Mn^{3+} ions interact with Co_3O_4 nanoparticles, which result to an increase of the lattice parameter as Mn content increased. This

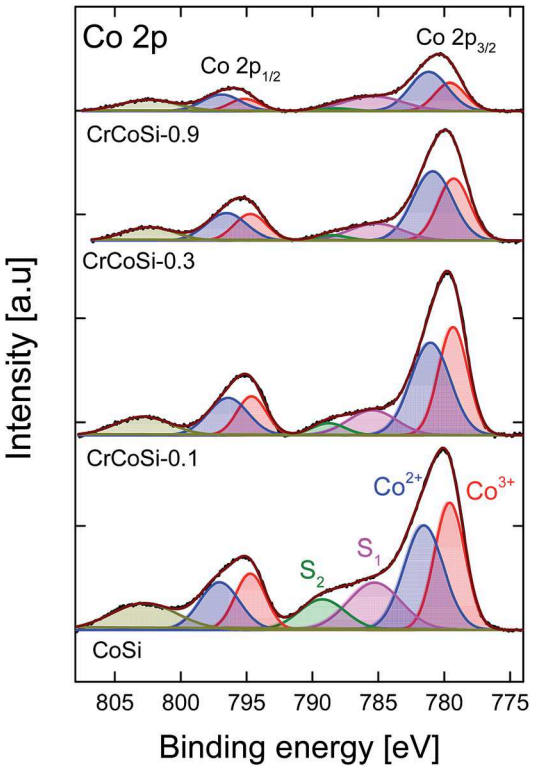

Fig. 5 Co2p spectra recorded from CoSi and CrCoSi samples with different Cr/Co (Cr/Co = 0.1, 0.3, 0.9) molar ratios.

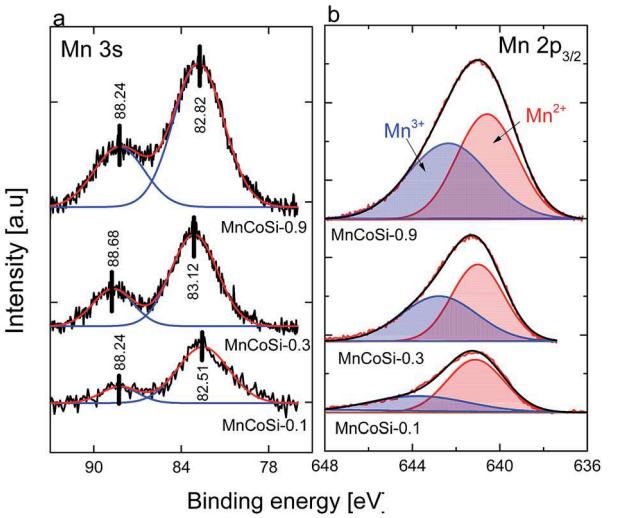

Fig. 6 XPS analysis of MnCoSi samples with different Mn/Co (Mn/Co = 0.1, 0.3, 0.9) molar ratios: (a) fitted Mn3s photoelectron peaks, (b) fitted Mn2p3/2 photoelectron peaks.

assumption is supported by two explanations: first, the substitution of Co^{2+} by Mn^{2+} in the tetrahedral site of the spinel Co_3O_4 can be ruled out as the difference in ionic radii between Co^{2+} (0.65 pm) and Mn^{2+} (0.67 pm) is negligible when considering Co^{3+} (0.54 pm) and Mn^{3+} (0.65 pm). Second, in $Mn_xCo_{3-x}O_4$ ($0 < x < 3$) systems, the face centered cubic *Fd3m* spinel-type solid has been reported to be formed in the compositional range of $x < 1.5$ (*i.e.* Mn/Co < 1) with a lattice parameter increasing from 0.807 nm ($x = 0$) to 0.8321 nm ($x = 1.5$) due to the substitution of Co^{3+} by Mn^{3+}.[25] The substitution of Co^{2+} by Mn^{2+} in the tetrahedral sites have been reported to occur only in the Mn-rich region ($x > 1.7$ *i.e.* Mn/Co > 1.3), which exhibit a tetragonal $I4_1/amd$ spinel type phase.[25] In this work, all MnCoSi samples (Mn/Co: 0.1–0.9) showed a face centered cubic *Fd3m* spinel-type phase with increasing lattice parameter from 0.808 nm (Mn/Co = 0) to 0.825 (Mn/Co = 0.9). Fig. 7 shows the Cr2p spectra for CrCoSi powders with different Cr/Co molar ratios.

The spectra were resolved in two peaks with binding energy of 576.73 eV and 578.2 eV corresponding to Cr^{3+} and Cr^{6+}, respectively.[28] The fitted Cr^{6+}/Cr^{3+} ratio, as shown in Table S5,† decreased from 0.68 to 0.52 with an increase in Cr content. As Cr^{6+} ions have been reported to be surface-only species,[29] we believe that the decrease in Co^{3+}/Co^{2+} ratio can only be ascribed to the substitution of Co^{3+} by Cr^{3+} ions. However, as for MnCoSi samples, the presence of amorphous Cr^{3+} species in the silica matrix cannot be ruled out as $Cr(NO_3)_3 \cdot 9H_2O$ was used as starting precursor.

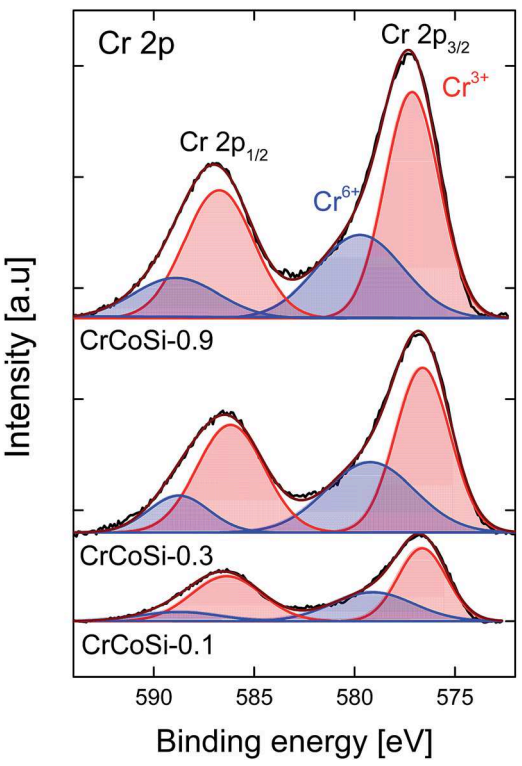

Fig. 7 Cr2p spectra recorded from CrCoSi samples with different Cr/Co (Cr/Co = 0.1, 0.3, 0.9) molar ratios.

Structural (FTIR) analysis

Fourier transform infrared spectroscopy was performed to assess the changes in the silica matrix induced by the variation in composition of binary Cr–Co and Mn–Co oxides. The FTIR spectra of CoSi and XCoSi (X = Mn, Cr) samples in the typical region of 900–1300 cm^{-1} are displayed in Fig. 8(a) and (b). Upon doping with single cobalt oxide and binary Mn–Co and Cr–Co oxides some variations in the shape and the frequency of the Si–O–Si asymmetric stretching band can be observed. This indicates that the insertion of these oxides, with different X/Co molar ratios, in the silica matrix induces changes in the structure of the siloxane network. To get more insights into these chemical changes, the Si–O–Si absorption band of CoSi and MnCoSi samples has been deconvoluted by means of five Gaussian contributions as shown in Fig. S3.† The peak at 950 cm^{-1} (1) represents the Si–OH bending vibration and the four other peaks (2–5) are attributed to Si–O–Si stretching modes with different bond angles.

According to the literature,[30,31] the peak centered at around 1042 cm^{-1} is assigned to Si–O–Si small rings, while the peaks centered at around 1079, 1150 and 1220 cm^{-1} are attributed to Si–O–Si–OH opened small rings with a terminal OH– group, Si–O–Si larger rings and Si–O–Si–OH opened larger rings with a terminal OH– group, respectively. Smaller rings refer to the stretching of Si–O–Si bonds in a network structure with bond angles ≤144°, while larger rings refer to the stretching of Si–O–Si bonds in a cage structure with bond angles ≥150°.[32]

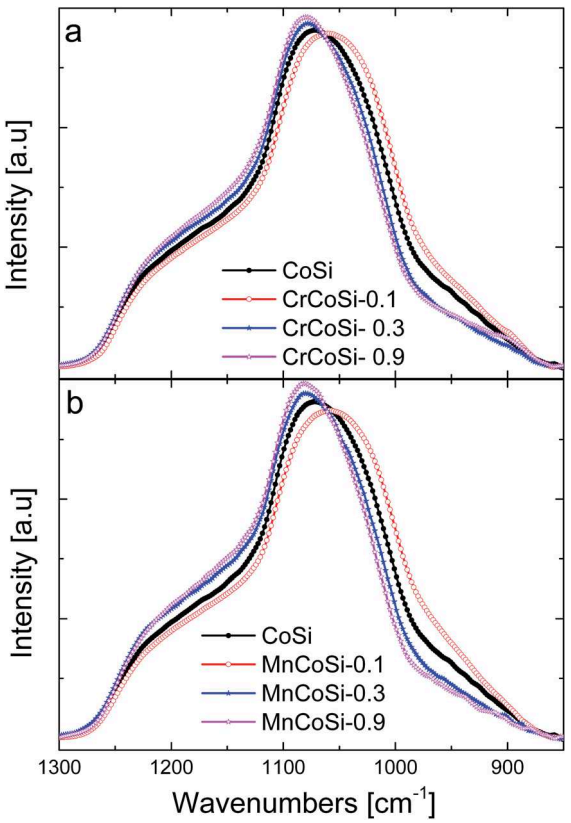

Fig. 8 FTIR spectra of all samples in the region 850–1300 cm^{-1}.

This means that, the smaller the bond angle, the higher density of the network and the lower the peak wavenumber would be. Fig. 9(a) displays the frequency shift of the most intense peak corresponding to Si–O–Si small rings (peak 2 in Fig. 9) as a function of the metal oxide composition.

The CoSi sample showed a Si–O–Si vibrational mode at 1042 cm^{-1}, which decreases to 1035 cm^{-1} as the X/Co (X = Cr or Mn) molar ratio increases to 0.10. This shift to lower wavenumbers indicates a decrease in the bonding angle *i.e.* an improvement of density of the silica network, which is in line with the gas permeation results. Further increase of the X/Co ratio enables a shift of the Si–O–Si peak to higher wavenumbers. For example, samples with X/Co molar ratios of 0.3 and 0.9 show a vibrational frequency value higher than that of the single CoSi sample because of a less dense silica network. More information on the changes in the silica structure was also obtained by investigating the evolution of the "small rings/large rings" area ratio *i.e.* the variation of the peak area [(2 + 3)/(4 + 5)] ratio as a function of the doping content (Fig. 9(b)). The binary XCoSi-0.1 samples show a higher value of the "Ring/Cage" ratio compare with that of the single oxide CoSi sample. However, this ratio drastically decrease to very low values for XCoSi-0.3 and XCoSi-0.9 samples, indicating an increase of the concentration of large siloxane rings. These results are in line with the behavior of the H_2/N_2 permeance ratio as shown in Fig. 2(c).

Fig. 9(c) displays the evolution of the silanol-to-siloxane peak area ratio as a function of X content. This corresponds directly to the trends observed in Fig. 9(b) and 2(c). Increasing the X/Co content from 0.1 to 0.9 enables a decrease of the concentration of Si–OH groups at the expense of Si–O–Si groups. Therefore, the decrease of the H_2/N_2 permeation ratio can only be ascribed to the formation of larger siloxane rings, which is more likely to occur *via* condensation reactions. Note that binary XCoSi samples with X/Co molar ratio of 0.1 display a higher concentration of Si–OH compared to the single CoSi sample. This is not surprising as the presence of Si–OH groups in the silica network is well-known to induce molecular sieve structures with narrow pore sizes.

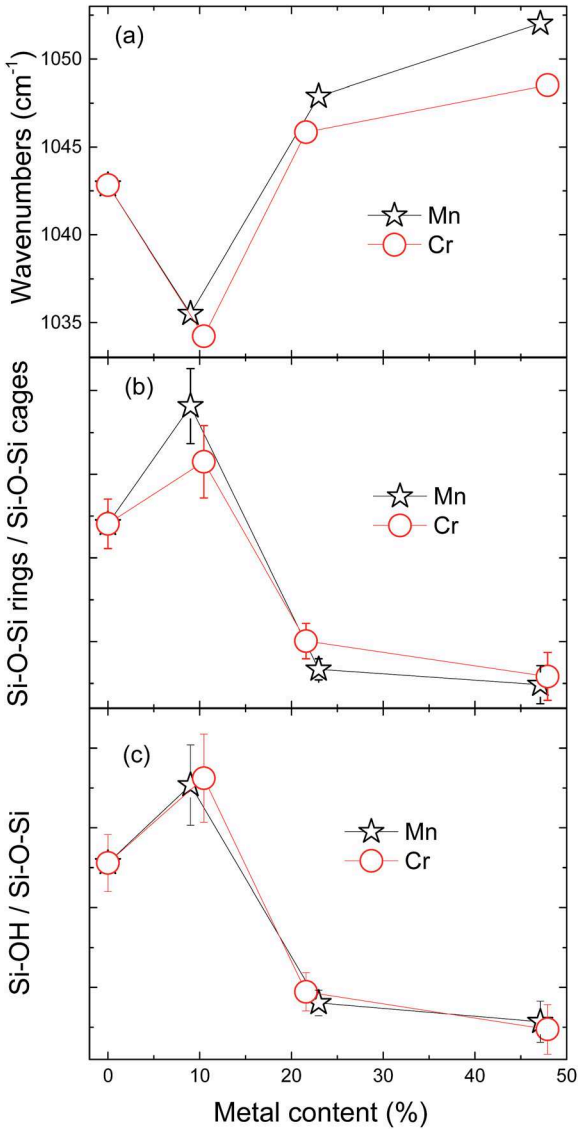

Fig. 9 (a) Frequency shift of the Si–O–Si small ring and variation of the peak area ratios (b) Si–O–Si rings/Si–O–Si cages and (c) Si–OH/Si–O–Si as a function of the X/Co (X: Mn, Co) molar ratio.

Conclusions

In this study, the sol–gel method was used for the preparation of several binary Co-X oxides-doped silica membranes (X: Mn, Cr) with different X/Co molar ratio (X/Co: 0.1, 0.3, 0.9) while keeping constant the total metal-to-silicon molar ratio ((X + Co)/Si = 0.5). Single gas permeation tests were performed at 200 °C to determine the effect of binary Co-X oxide composition on the amorphous silica network. In addition, several characterization techniques such as XPS, XRD, FTIR and TEM were used to evaluate the changes in the silica matrix induced by the variation in composition of these binary oxides. The H_2/N_2 permeance ratio decreased for more than one order of magnitude with an increase in X/Co molar ratio from 0.1 to 0.9 due to the formation of large pore sizes. On the other hand, membranes prepared with the X/Co molar ratio of 0.1 showed a H_2/N_2 permeance ratio, which was approximately twice higher than that of the single cobalt oxide-doped silica membrane (CoSi), indicating a densification of the silica network. Upon doping with Mn and Cr, the lattice parameter significantly increased due to the substitution of Co^{3+} by larger cations Mn^{3+} and Cr^{3+} in octahedral sites of the spinel Co_3O_4. This resulted to the formation of $Mn_xCo_{3-x}O_4$ and $Cr_xCo_{3-x}O_4$ oxide nanocrystals within the silica matrix. However, the presence of amorphous (Co, Mn and Cr) species was also demonstrated. The formation of larger pore sizes at high X content was ascribed to the formation of bigger siloxane rings *via* condensation reactions. The presence of narrow pore sizes at low X content was attributed to the high concentration of silanol groups, more likely influenced by the concentration of amorphous species (Mn, and Cr) in the silica matrix.

Acknowledgements

One of the authors, Patrick H. Tchoua Ngamou, acknowledges a Fellowship of the Alexander von Humboldt (AvH) Foundation for his postdoctoral stay in Germany.

References

1 J. Zang, Y. Ding, Y. Pei, J. Liu, R. Lin, L. Yan, T. Liu and Y. Lu, *React. Kinet., Mech. Catal.*, 2014, **112**, 159.
2 C.-C. Lin, Y. Guo and J. Vela, *ACS Catal.*, 2015, **5**, 1037.
3 R. Xie, C. Wang, L. Xia, H. Wang, T. Zhao and Y. Sun, *Catal. Lett.*, 2014, **144**, 516.
4 C. Cantalini, M. Post, D. Buso, A. Guglielmi and A. Martucci, *Sens. Actuators, B*, 2005, **108**, 184.
5 O. A. Fouad, G. A. M. Ali, M. A. I. El-Erian and S. A. Makhlouf, *Nano*, 2012, **7**, 1.
6 R. Igi, T. Yoshioka, Y. H. Ikuhara, Y. Iwamoto and T. Tsuru, *J. Am. Ceram. Soc.*, 2008, **91**, 2975.
7 D. Uhlmann, S. Smart and J. C. D. da Costa, *Sep. Purif. Technol.*, 2010, **76**, 171–178.
8 L. Liu, D. K. Wang, D. L. Martens, S. Smart, E. Strounina and J. C. D. da Costa, *RSC Adv.*, 2014, **4**, 18862–18870.
9 L. Liu, D. K. Wang, D. L. Martens, S. Smart and J. C. D. da Costa, *J. Membr. Sci.*, 2015, **475**, 425–432.
10 V. Boffa, G. Magnacca, L. B. Jorgensen, A. Wehner, A. Doernhoefer and Y. Yue, *Microporous Mesoporous Mater.*, 2013, **179**, 242–249.
11 D. Uhlmann, S. Smart and J. C. D. da Costa, *J. Membr. Sci.*, 2011, **380**, 48–54.
12 J. Wang and T. Tsuru, *J. Membr. Sci.*, 2011, **369**, 13–19.
13 A. Darmawan, S. Smart, A. Julbe and J. C. D. da Costa, *Materials*, 2011, **4**, 448–456.
14 Y.-F. Han, F. Chen, Z. Zhong, K. Ramesh, L. Chen and E. Widjaja, *J. Phys. Chem. B*, 2006, **110**, 24450–24456.
15 X. Z. Zhang, Y. H. Yue and Z. Gao, *Catal. Lett.*, 2002, **83**, 19–25.
16 B. Ballinger, J. Motuzas, S. Smart and J. C. D. da Costa, Palladium cobalt binary doping of molecular sieving silica membranes, *J. Membr. Sci.*, 2014, **451**, 185–191.
17 B. Ballinger, J. Motuzas, S. Smart and J. C. D. da Costa, *J. Membr. Sci.*, 2015, **489**, 220–226.
18 A. Darmawan, J. Motuzas, S. Smart, A. Julbe and J. C. D. da Costa, *J. Membr. Sci.*, 2015, **474**, 32–38.
19 N. Bahlawane, P. H. T. Ngamou, V. Vannier, T. Kottke, J. Heberle and K. Kohse-Hoeinghaus, *Phys. Chem. Chem. Phys.*, 2009, **11**, 9224–9232.
20 T. van Gestel, F. Hauler, M. Bram, W. A. Meulenberg and H. P. Buchkremer, *Sep. Purif. Technol.*, 2014, **121**, 20–29.
21 M. C. Biesinger, B. P. Payne, A. P. Grosvenor, L. W. M. Lau, A. R. Gerson and R. S. C. Smart, *Appl. Surf. Sci.*, 2011, **257**, 2717–2730.
22 K. Morishige, *J. Phys. Chem. C*, 2011, **115**, 9713–9718.
23 S. Esposito, M. Turco, G. Ramis, G. Bagnasco, P. Pernice, C. Pagliuca, M. Bevilacqua and A. Aronne, *J. Solid State Chem.*, 2007, **180**, 3341–3350.
24 H. Bordeneuve, C. Tenailleau, S. Guillemet-Fritsch, R. Smith, E. Suard and A. Rousset, *Solid State Sci.*, 2010, **12**, 379–386.
25 A. Restovic, E. Rios, S. Barbato, J. Ortiz and J. L. Gautier, *J. Electroanal. Chem.*, 2002, **522**, 141–151.
26 W. Wei, W. Chen and D. G. Ivey, *Chem. Mater.*, 2008, **20**, 1941–1947.
27 B. Djurfors, J. N. Broughton, M. J. Brett and D. G. Ivey, *Acta Mater.*, 2005, **53**, 957–965.
28 J. Chen, X. Zhang, H. Arandiyan, Y. Peng, H. Chang and J. Li, *Catal. Today*, 2013, **201**, 12–18.
29 J. Sloczynski, J. Janas, T. Machej, J. Rynkowski and J. Stoch, *Appl. Catal., B*, 2000, **24**, 45–60.
30 A. Milella, M. Creatore, M. C. M. van de Sanden and N. Tomozeiu, *J. Optoelectron. Adv. Mater.*, 2006, **8**, 2003–2010.
31 A. Milella, M. Creatore, M. A. Blauw and M. C. M. V. de Sanden, *Plasma Processes Polym.*, 2007, **4**, 621–628.
32 A. Grill and D. A. Neumayer, *J. Appl. Phys.*, 2003, **94**, 6697–6707.